Influence of microstructural parameters on the mechanical properties of oxide dispersion strengthened Fe-14Cr steels

M. Dadé, J. Malaplate, J. Garnier, Frédéric de Geuser, F. Barcelo, P. Wident, A. Deschamps

Influence of microstructural parameters on the mechanical properties of oxide dispersion strengthened Fe-14Cr steels

M. Dadé[a,1], J. Malaplate[a,*], J. Garnier[a], F. De Geuser[b,c], F. Barcelo[a], P. Wident[a], A. Deschamps[b,c]

[a] *DEN-Service de Recherches Métallurgiques Appliquées, CEA, Université Paris-Saclay, F-91191 Gif-Sur-Yvette, France*

[b] *Univ. Grenoble Alpes, SIMAP, F-38000 Grenoble, France*

[c] *CNRS, SIMAP, F-38000 Grenoble, France*

* *Correponding author E-mail address : joel.malaplate@cea.fr*

[1] *Present address: MINES ParisTech, PSL Research University, Centre des Matériaux, CNRS UMR 7633, BP 87, 91003, Evry Cedex, France*

ABSTRACT

The effect of microstructural parameters on the microstructure, tensile properties from room temperature to 800°C and creep properties at 650°C has been investigated in a 14%Cr oxide dispersion strengthened (ODS) steel. Combining a control of oxide addition, consolidation route and thermo-mechanical processing, the different parameters of the microstructure have been varied systematically, namely the size and volume fraction of oxide nano-precipitates, the grain size and the dislocation density.

The volume fraction of nano-precipitates is shown to influence the tensile strength throughout the temperature range, whereas a change in precipitate size influences only the low temperature behavior. The effect of grain size is shown to be similar to that of precipitation strengthening. A recrystallized microstructure is shown to improve the ductility of the ODS steel while not degrading the strength or creep resistance. The material processed by hot extrusion presents improved strength and reduced creep rate as compared to that consolidated by hot isostatic pressing. This difference is attributed to the long-range internal stress resulting from the high dislocation density, stabilized by the oxide nano-precipitates.

A strength model is presented, and validated on every material using the quantitative microstructural parameters obtained by combination of electron back-scattered diffraction, transmission electron microscopy and small-angle X-ray scattering.

Keywords: ODS steel, Microstructural parameters, Tensile tests, Creep tests, Modeling

1. INTRODUCTION

Oxide dispersion strengthened (ODS) steels have received considerable attention in the last 10 years owing for their exceptional stability at high temperature and very good resistance to high temperature creep. In particular, the combination of creep resistance in the 500-700°C temperature range and low swelling under irradiation of ferritic / martensitic ODS steels makes them attractive candidates for the cladding fuel of sodium cooled fast reactors [1].

The nanometer size oxide particles providing these properties are obtained through a powder metallurgy process. The steel powder is milled with (Y,Ti) oxide powder under protective atmosphere [2], which drives Y, Ti

and O in solid solution in the ferritic matrix. Then, the powder milled is canned and consolidated, using Hot Extrusion (HE), Hot Isostatic Pressing (HIP) or Spark Plasma Sintering (SPS) [3].

The microstructure resulting from the consolidation process is very complex. The combination of high-energy ball milling with the presence of a large volume fraction of nanometer-scale particles results in a very small grain size, partly sub-micrometric [4] and frequently bi-modal [5]. In addition, a residual large quantity of dislocations can be present after consolidation, particularly after hot extrusion, due to low rates of recovery [6]. The two main phases usually considered in (Y+Ti) added steels are $Y_2Ti_2O_7$ and Y_2TiO_5, and a consensus is rising about the dominant role of the pyrochlore phase [7-9]. The variety of microstructures depending on material composition and processing route leads to a wide range of mechanical properties and their evolution with temperature [10-12].

Different studies have evaluated the effect of microstructural parameters, such as the volume fraction of nanoparticles [13-15] or the nature of chemical elements present in solid solution [16-17], on the mechanical properties. These studied materials were processed by hot extrusion, with a resulting very strong morphological and crystallographic texture oriented along the extrusion direction (α fiber) [18-19]. This anisotropy coupled with the complexity of steel microstructures complicates the understanding of the influence of each microstructural parameter on the mechanical behavior. Although a number of models have been proposed to evaluate the microstructure / properties relationship both at room and at high temperature [11, 20-23], there is still a lack of quantitative understanding of the effect of the specific nature of the ODS microstructure and a clear description of the mechanical behavior as a function of temperature is also missing. In particular, the respective role of precipitate size, volume fraction, grain size on the low and high temperature strength and creep resistance remain unclear.

In this context, the aim of the present paper is to present an evaluation of the microstructure and mechanical properties of several model ODS steels where a particular effort has been made to change independently the different parameters of the microstructure. In order to simplify the microstructure, the materials have been mostly consolidated by hot isostatic pressing, which ensures an isotropic morphological and crystallographic texture. They are all based on the same composition, with 14%Cr and 1%W, ensuring a fully ferritic microstructure. The volume fraction of oxide particles has been varied by adding different amounts of Y, Ti and O. The size of particles has been varied at constant volume fraction by heat treating the consolidated material at high temperature. The grain size has been varied at constant precipitate size by applying the same heat treatment, with a prior cold deformation

that induces recrystallization. In addition, a comparison has been made with a material processed by hot extrusion with a similar oxide particle distribution, thus containing a higher density of dislocations.

The different parameters of the microstructure of these different materials have been quantified by a combination of experimental methods. The grain size distribution has been evaluated by Scanning Electron Microscope (SEM) observations coupled with an Electron BackScatter Diffraction (EBSD), and for the smallest ones using Automated Crystal Orientation Mapping (ACOM) in a Scanning Transmission Electron Microscope (STEM). The dislocation density has been evaluated by Transmission Electron Microscopy (TEM). The precipitate size and volume fraction has been evaluated by Small-Angle X-Ray Scattering (SAXS) and TEM.

The mechanical properties have been studied by performing tensile tests from room temperature up to 800°C. In addition, creep tests have been performed at 650 and 700°C. Based on the microstructure evaluation, a model for the low temperature strength and a rationalization of the high temperature strength will finally be presented.

2. MATERIALS AND METHODS

The ferritic ODS steels were produced by mechanical alloying of the mixture of a pre-alloyed powder and Y_2O_3 and TiH_2 powders. A Union Process SD01 attritor has been used for ball milling under argon atmosphere for 10h. The ball-to-powder ratio was 15:1. On the contrary, the as-received pre-alloyed powder used for the un-strengthened ferritic steel has not been milled to avoid any residual contaminations of Y or Ti. Powders, whether in a ball-milled state or in an atomized state, were canned and annealed to reduce oxygen content (2h at 300°C-400°C under secondary vacuum). Then, they were consolidated at 1100°C under two different processes: hot isostatic pressing (HIP) (1900 bars, 2h) and hot extrusion (HE) with a 13:1 reduction section in cross-sectional area and an extrusion rate of 25 $mm.s^{-1}$. Then, the extruded rod was annealed at 1050°C for 1h.

The alloys' compositions are given in Table 1. The base alloy composition is common to every alloy, namely approximately 14% Cr and 1% W. To study the effect of the volume fraction of nanoparticles, four different steels have been elaborated using the HIP consolidation: an un-strengthened material (**US**) with no addition of Ti or Y, a low strengthened material (**LS**) with a low addition of oxides, a reference material (**Ref**) with an addition of oxides typical of most studies of the literature and a high-strengthened material (**HS**) with a higher amount of oxides addition. Two other materials have been obtained based on a recent study [24]: a material with coarse precipitates

(**CP**) having the same addition of Ti, Y and O than the reference material but with a heat treatment subsequent to HIP of 1h at 1400°C, and a recrystallized material (**Rc**) having the same addition of Ti, Y and O than the reference material but based on the HE consolidation route, with a cold deformation of 40% by compression followed by a heat treatment of 1h at 1400°C. Finally, a hot extruded material **(HE)**, containing the same amount of addition as the reference material, was elaborated to study the effect of dislocation density, since this consolidation route is expected to provide a higher dislocation density [25-26] as compared to the HIP route.

	Cr	W	Ti	Y	Al	O
US	13.78 ± *0.25%*	1.00 ± *0.25%*	-	-	0.01 ± *0.005%*	0.059 ± *0.003%*
LS	14.25 ± *0.25%*	1.06 ± *0.03%*	0.08 ± *0.01%*	0.06 ± *0.01%*	0.042 ± *0.005%*	0.103 ± *0.005%*
Ref	14.51 ± *0.25%*	0.93 ± *0.02%*	0.22 ± *0.01%*	0.16 ± *0.01%*	0.049 ± *0.005%*	0.081 ± *0.003%*
HE	14.18 ± *0.25%*	0.95 ± *0.02%*	0.26 ± *0.01%*	0.18 ± *0.01%*	0.046 ± *0.005%*	0.078 ± *0.003%*
HS	13.94 ± *0.25%*	0.75 ± *0.02%*	0.91 ± *0.02%*	0.65 ± *0.02%*	0.034 ± *0.005%*	0.25 ± *0.10%*
Rc	14.18 ± *0.25%*	0.95 ± *0.02%*	0.26 ± *0.01%*	0.18 ± *0.01%*	0.046 ± *0.005%*	0.078 ± *0.003%*
CP	14.51 ± *0.25%*	0.93 ± *0.02%*	0.22 ± *0.01%*	0.16 ± *0.01%*	0.049 ± *0.005%*	0.081 ± *0.003%*

Table 1. Content (wt%) of the different elements by several destructive chemical analysis (spectrometry and absorption measurements) for the different steels. Fe is in balance.

EBSD analyses were realized with a Field Emission Gun SEM JEOL JSM-7001FLV apparatus with a voltage of 20 kV. Orientation maps were taken with a step of 0.374 µm. Samples for EBSD were mechanically mirror polished followed by electropolishing, using an electrolyte containing 70% of ethanol, 20% of ethylene glycol monobutyl ether and 10% of perchloric acid, used at 5°C with a tension of 27 V during 30 seconds.

TEM investigations were carried out on a JEOL 2010F microscope operating at 200 kV, on disks prepared by conventional mechanical polishing followed by double-jet electropolishing with the same electrolyte as for the EBSD preparation. The tension for TEM thin samples is 30 V with an intensity of 170 mA. Automated Crystal Orientation mapping (ACOM) in a TEM was made using the ASTAR system in scanning mode [27].

SAXS measurements were performed on foils of thickness in the range of 30-70 µm. The X-ray source was a rotating anode, working with the wavelength K_α of molybdenum. The X-ray signal was detected using a 2D PILATUS detector, whose settings allowed the removal of the constant fluorescence background from Cr and Fe. The sample-to-detector distance, 1.276 m, was chosen to cover the range of scattering vectors (0.215 nm^{-1} to 6.14 nm^{-1}). The scattering vector is given by $q = \frac{4\pi}{\lambda} \times \sin\theta$ with λ the wavelength and θ the half scattering angle [28].

Tensile tests have been carried out in air at temperature ranging from the room temperature to 800°C. They were strain controlled with a strain rate of 7.10^{-4} s^{-1} in an Instron tensile machine with a load cell of 2kN and equipped with a radiation furnace. The specimen temperature was measured by thermocouple. The tensile specimen geometry has a 6 mm gauge length and a 1.5 mm x 0.75 mm square section.

Constant-load creep tests were carried out in air at 650°C and 700°C using three geometries of cylindrical specimens of respective gauge / diameter dimensions (in mm): 4 / 20, 3 / 15 and 2 / 7. Creep samples of the **HE** material have been machined in the hot extrusion direction.

3. RESULTS

3.1. Microstructural characterization

3.1.1. Grain size distribution

Fig. 1 shows EBSD maps for each material. Out of these materials, the **US** material has a specific microstructure related to its consolidation, which was made directly on the atomized powder (no milling), and does not contain any oxide nanoparticles. The resulting grain size is large, and in addition a significant fraction (~ 19%) of non-indexed areas are present at this scale. EBSD maps at higher magnification showed that these areas are constituted from martensite blocks. The origin of this martensite is related to the content of nitrogen and carbon, present in solid solution and which were not trapped by titanium or chromium to form carbides or nitrides.

As shown in Fig. 1, the grain structures of all ODS steels present similar features. These low resolution EBSD maps evidence the presence of a wide grain size distribution, with the presence of relatively large grains of size larger than 10 µm, and non-indexed areas. These areas are made of very small grains, which have been systematically imaged at higher magnification for the evaluation of grain size distribution as shown in Fig. 2 for the specific case of the **Ref** alloy. High-resolution EBSD and ACOM-TEM maps show the presence of grains of size well below 1 µm, in the range 100-300 nm. Such a bi-modal grain size distribution is expected in ODS steels after ball-milling and consolidation [29-32]. For the alloys consolidated by HIP, the overall grain structure is isotropic, with very little crystallographic texture, although locally some elongated large grains can be observed, e.g. for the **LS** material, probably inherited from the ball milling at powder grain scale. In contrast, the alloy consolidated by hot extrusion presents a much more oriented microstructure, consistent with the literature [24]. This material has a

strong texture, which has been presented elsewhere [24]. As expected, when the amount of oxide forming elements is increased, the relative fraction of small grain population increases, confirming that the presence of these grains is related to the Zener drag exerted on the grain boundaries by the nanometer-size oxide particles.

The material containing coarse precipitates (**CP**) has been heat-treated 1h at 1400°C, so that it is necessary to evaluate how much this heat treatment has changed its grain microstructure. As discussed in more details in [24] and illustrated in Fig. 1, the grain microstructure is little affected by this heat treatment, which illustrates the remarkable stability of the sub-micrometer size grains in these materials. However, a difference on the average grain size can be noted compared to the **Ref** material, which is related to the fact that the **CP** material is not from the same batch as the **Ref** material. However, this difference being small, it will be possible to evaluate specifically the role of the size of oxide particles without interference with a major change of grain size. Last, the recrystallized material (**Rc**) was consolidated by hot extrusion, cold deformed by 40% and heat treated also for 1h at 1400°C. As illustrated in Fig. 1 this procedure makes it possible to achieve a recrystallized microstructure with a grain size of the order of 10 µm, while the oxide precipitates have a size similar to that in the **CP** material, making it possible to evaluate the effect of grain size independently from a change of precipitate characteristics, although some texture change has occurred as shown in [24].

From EBSD maps realized at different scales, grain size distributions have been measured with grain boundaries defined by a misorientation angle higher or equal to 5°. They are shown for all materials in supplementary material, and the average grain size calculated from these distributions is given in Table 2. The calculated mean grain size of the HIPed and the recrystallized materials equates to an equivalent diameter. On the contrary, the mean grain size of the **HE** material has been estimated using a line-intercept method due to the anisotropic grain morphology. Thus the mean grain size of the **HE** material given in Table 2 corresponds to length x width.

3.1.2. Precipitation state

The different alloys contain some large particles with a mean radius of the order of 100 nm that were observed by TEM in the different model materials. As summarized by Sakasegawa et al. [33], the chemistry of these coarse precipitates varies between Ti-O and Al-O depending of the material.

In this study, we focused the characterization on the precipitates at the nanometer scale, which are controlling the mechanical properties. These precipitates were studied using SAXS and TEM. Fig. 3a and b show TEM images

for two alloys (**Ref** and **Rc**). In the **Ref** material, a homogeneous fine-scale distribution of precipitates is evidenced. Observations in large and very small grains did not show evidence of a significant difference in precipitate size distribution. In the **Rc** material, the heat treatment at 1400°C results in a size increase of the precipitates, accompanied by a shape change from cubic to cuboidal. Similar shape and weak size difference of precipitates were observed in the **CP** material. These cubic or cuboidal shapes are not expected to affect the modeling results.

Fig. 4 shows the SAXS curves for every alloy in Kratky representation after subtraction of a constant scattering contribution and of the contribution of the asymptotic contribution of large particles and crystalline defects (q^{-n} contribution with n between 3 and 4). In these Kratky plots, the integrated area (integrated intensity Q_o) is directly related to the volume fraction of nanometer-scale precipitates through a contrast factor, and the position of the maximum is inversely proportional to the average precipitate size [34]. The data before subtraction of this large particle contribution can be found in supplementary material.

As expected, the lack of small precipitates is evidenced on the **US** SAXS signal. The **LS** material shows only a small contribution of nano-scale precipitate. The **Ref** and **HS** material show a strong signal from nanoscale precipitates which is, as expected, much more intense in the **HS** material. The **HE** material presents a similar behavior as that of the **Ref** material, however with a much stronger contribution at small scattering vectors, which arises from the higher dislocation density. In fact, after subtraction of the q^{-n} contribution, the nanoscale precipitate contributions of the **Ref** and **HE** materials are almost identical (Fig. 4). Both the **CP** and **Rc** materials show a SAXS signal at smaller scattering vectors, illustrating the oxide coarsening. The nanoscale precipitate distribution is close in these two materials, despite the prior deformation and recrystallization phenomenon in the **Rc** material.

Following the procedure explained in details in [28] the SAXS signal was modeled using the combination of the low-q contribution arising from the large particles present in the microstructure, a log normal distribution of spheres, and a constant background. In this way, the mean radius of the precipitates and the dispersion parameter, which corresponds to a measurement of the width of the particle size distribution [28], has been obtained. A very good agreement between the SAXS-determined precipitate size and that obtained from TEM measurements has been found. A complete description of the comparison between SAXS and TEM results can be found in the supplementary material. For comparing the different materials, we chose in the following to consider the mean radius determined by SAXS (see Table 2) due to the more statistical nature of the measurement.

The integrated intensity of the hardening precipitates was obtained by integration of the contribution of the nanoscale precipitates to the SAXS intensity, and converted to volume fraction in the same way as in [28]. In order to do so, the contrast in electron density between the matrix and the precipitates needs to be known. As discussed by [35], $Y_2Ti_2O_7$ and Y_2TiO_5 have almost the same electronic density, so that they do not have to be distinguished for their contribution to the SAXS intensity. In the following, we chose to consider a mixture at 50% of both phases, and the resulting volume fractions are given in Table 2.

The table shows that the current alloy design strategy was successful in changing separately the precipitate volume fraction and the precipitate size. In the materials with different additions of oxide forming elements, we obtain large changes in precipitate volume fraction, with moderate changes in precipitate size. The **HE** and **Ref** materials have very similar precipitate characteristics, whereas the 1400°C heat treatment, with or without prior cold work, changed the precipitate size at almost constant volume fraction. The small difference between volume fraction of **HE** and **Rc** materials is probably due mostly to uncertainties of SAXS measurements. A small increase of the volume fraction towards the equilibrium state (Gibbs-Thomson effect) could be induced by the Ostwald ripening mechanism. Still, as expected, the material with the highest amount of oxide forming elements shows the smallest precipitate size, and this effect will have to be taken in consideration for modeling.

3.1.3. Dislocation density

For every material, the average dislocation density (ρ) has been determined by using the line-intercept method in the same way as in [36] on bright field and dark field TEM pictures. The average dislocation density for each material is given in Table 2.

The dislocation densities of **LS**, **Ref** and **HS** materials are nearly the same. On the contrary, the **HE** material presents a higher dislocation density, which is due to the 13:1 section reduction during hot extrusion. Concerning the **CP** material, the dislocation density is low following the annealing at 1400°C. Due to recrystallization, the dislocation density of **Rc** material should be negligible. However, small grains, which have not recrystallized, still contain dislocations. Thus, the dislocation density of the **Rc** material has been estimated using the ratio of remaining small grains (10% with a mean dislocation density of 5.5 10^{-13} m^{-2}).

Table 2 also shows that the dislocation density of the **US** material is very low compared to the HIPped ODS steels.

	US	LS	Ref	HE	HS	CP	Rc
Mean grain size (µm)	27.6 ± *0.5*	4.3 ± *0.5*	6.5 ± *1.2*	1.2 x 0.4 ± *1.1 x 0.8*	1.8 ± *0.05*	4.5 ± *1.0*	9.5 ± *0.6*
Mean radius (nm)	-	1.56 ± *0.34*	1.27 ± *0.03*	1.31 ± *0.09*	0.9 ± *0.1*	3.1 ± *0.5*	2.55 ± *0.45*
Dispersion parameter	-	0.4	0.24	0.21	0.5	0.32	0.32
Q_0 (Å^{-6})	-	0.05 ± *0.005*	0.079 ± *0.008*	0.082 ± *0.008*	0.156 ± *0.016*	0.082 ± *0.008*	0.097 ± *0.01*
Volume fraction (%)	-	0.31% ± *0.03*	0.52% ± *0.05*	0.53% ± *0.05*	1.03% ± *0.1*	0.53% ± *0.05*	0.62% ± *0.06*
Dislocation density (m^{-2})	5 10^{12} ± *2 10^{12}*	1 10^{14} ± *4 10^{13}*	9.7 10^{13} ± *3.9 10^{13}*	5 10^{14} ± *2 10^{14}*	2.5 10^{14} ± *1 10^{14}*	1 10^{13} ± *4 10^{12}*	5 10^{12} ± *2 10^{12}*

Table 2. Average grain size, particles size, volume fraction of nanoparticles and dislocation density of the different ODS steels.

3.2. Tensile properties at room temperature

The room temperature tensile properties of the model materials, including 0.2% yield strength (YS), ultimate tensile strength (UTS) and elongation-to-failure (ε_f), are listed in Table 3. The room temperature tensile curves tested at a strain rate of 7.10^{-4} s^{-1} are presented in Fig. 5a. As expected, the presence of oxide nanometer-scale precipitates drastically increases the strength of the alloy, from about 260 MPa without oxide precipitates to 1650 MPa for the largest amount of precipitates. This increase of yield stress comes along with a large reduction in ductility. In the **LS** and **Ref** materials the ductility is still reasonably large, between 15 and 20%, however the **HS** material presents a brittle character at room temperature.

Concerning the effect of particles size, the comparison between the **Ref** and **CP** materials shows a large loss of yield strength when the nanoparticles growth while the ductility does not seem to be impacted. The comparison between the **Rc** and **CP** materials, allowing to understand the effect of grain size, shows no difference on YS, UTS or ε_f. This suggests that there is no significant effect of grain size in this size range. However, Table 2 shows that the **CP** and **Rc** materials do not have exactly the same precipitate volume fraction, resulting in a different strength contribution from the precipitates, so that the similar yield strength observed between the **Rc** and **CP** materials may result from a compensation of differences in precipitate volume fraction and grain size.

As discussed in more details in [32, 37] and illustrated in Table 3, the **HE** material, tested in the axial direction, shows a higher YS, UTS and ε_f value than the **Ref** material. This difference may result from the morphologic and crystallographic texture. Furthermore, Table 2 shows a high dislocation density for the **HE** material, which increases the forest dislocation and internal back stress hardening.

	US	LS	Ref	HE	HS	CP	Rc
YS (MPa)	263 ± *5*	809 ± *5*	1085 ± *5*	1182 ± *5*	1646 ± *5*	736 ± *5*	739 ± *5*
UTS (MPa)	459 ± *5*	1059 ± *5*	1171 ± *5*	1257 ± *5*	1646 ± *5*	887 ± *5*	904 ± *5*
ε_f (%)	30 ± *0.5*	19 ± *0.5*	17 ± *0.5*	21 ± *0.5*	1 ± *0.5*	16 ± *0.5*	17 ± *0.5*

Table 3. Room temperature tensile properties of studied materials.

3.3. Effect of temperature on the tensile properties

All materials have been tested in tension in the temperature range 20-800°C. Fig. 5b shows the stress-strain curves at the different temperatures, at a strain rate of 7.10^{-4} s^{-1}, for the **Ref** material. From room temperature to 400°C, the material looses about 20% of yield strength, but the general shape of the stress-strain curve is not changed. Above 500°C, the yield strength continues to drop, and the stress-strain curves become completely flat. At 800°C, the yield strength becomes smaller than 200 MPa. The ductility is observed to follow a non-monotonic evolution with temperature. It goes through a maximum from 500 to 650°C before dropping sharply at 800°C.

The evolution of yield strength with temperature is summarized for every alloy in Fig. 6a. All alloys show qualitatively the same evolution as that observed in the **Ref** material, namely the yield strength drops slowly between room temperature and 400°C, then more sharply between 500 and 650°C, and then again more slowly until 800°C. At all temperatures, the order between the **HS**, **Ref**, **LS** and **US** materials remains the same, namely the higher the volume fraction of oxide precipitates, the higher the yield strength. However, the ratio between these yield strengths has a tendency to decrease with increasing temperature. A different situation is observed for the effect of precipitate size. The **Rc** and **CP** materials, containing larger precipitates, have a significantly lower yield stress at room temperature than **Ref**, but this difference cancels at 650°C and even slightly inverts at 800°C, showing that large precipitates may actually be favorable at higher temperature. The grain microstructure does not appear to play a major role on the yield stress as the **Rc** and **CP** materials show similar values throughout the temperature range. The most striking behavior is observed when comparing the **Ref** material to the same material processed by hot extrusion (**HE**). This last material shows a much lower decrease of the yield stress with temperature. Actually, the difference in yield strength (about 100 MPa) between the two materials is rather constant with temperature up to 800°C, where the **HE** material has the highest yield strength of every material studied.

The evolution of total elongation is given in Fig. 6b. Out of all materials, the **US** material shows the most specific evolution with temperature. Namely, its ductility increases monotonically with temperature, in accordance

with the material becoming softer. In contrast, every oxide reinforced material shows a non-monotonic evolution of total elongation, with a maximum of ductility ranging between 500 and 650°C. This maximum is most pronounced for the **LS** material which shows the highest elongation at 650°C, and for the **HS** material, whose brittle behavior changes to a relatively high ductility also at 650°C. The two materials with larger precipitates show a much less pronounced ductility peak. At the highest temperature of 800°C, all oxide containing materials show a low ductility (not more than 10%), but it is worth noticing that the recrystallized material (**Rc**) shows a significantly higher ductility than the other materials containing the same volume fraction of precipitates, actually more representative of the **LS** material. If we now evaluate the effect of the processing route, we can see that the **HE** and **Ref** materials show the same evolution, contrarily to that seen for yield strength.

3.4. Creep tests results

Finally, all materials were tested in creep. The temperature of 650°C was chosen, being typical of an upper temperature for the application of these materials in future fast neutron nuclear reactors. The secondary creep rates are shown in Fig. 7a. The unreinforced material shows a classical 5 exponent for the stress dependence of creep rate, as expected from a material free of hardening precipitates. All other materials show much higher exponents, ranging from 10 to 23. These apparent exponents are typical of precipitation-reinforced alloys [38] and correspond to the transition from a threshold stress below which the creep rate falls to zero. Even though the range of stresses investigated was not sufficient to measure with reasonable precision the threshold stress for the different materials, a qualitative evaluation can be made by extrapolation with a secondary creep rate of 10^{-14} s^{-1} (Table 4). This threshold stress clearly increases with increasing volume fraction of oxide precipitates, from less than 40 MPa for the **LS** material to more than 100 MPa for the **HS** material. The three materials with identical volume fraction of oxide particles and similar processing route (**Ref**, **Rc** and **CP**) show similar results (Fig. 7a), within experimental uncertainty, suggesting that the volume fraction of the oxide precipitates is the main controlling parameter, more than their size or the grain size. However, the **HE** material shows a very different behavior, namely it presents creep rates comparable, even better, than the **HS** material, about four orders of magnitude lower than the **Ref** material. Translating into a difference of threshold stress, that of the **HE** material is about 100 MPa larger than that of the **Ref** material, which incidentally corresponds quite well with the constant difference of yield stress that was measured as a function of temperature (see Fig. 6a).

	LS	Ref	CP	Rc	HS	HE
Threshold stress (MPa)	32 ± 5	48 ± 5	80 ± 10	54 ± 10	102 ± 5	154 ± 5

Table 4. Estimation of the threshold stress of each material.

It is also of interest to evaluate the effect of microstructure, not only on the creep rate, but also on the lifetime under creep, which depends also on the strain to failure. The Larson Miller parameter (LMP) is a useful way to represent the lifetime [39] as a function of the applied stress. This representation is made in Fig. 7b for creep tests realized at 650 and 700°C. This figure shows that the materials can be separated in three groups; the lowest lifetimes at a given stress are observed for the **US** material, which means that the high ductility of this material is not sufficient to compensate the much higher creep rate. In the second group one finds every oxide reinforced material except the **HS** and **HE** material, due to their particularly low creep rate. Again, a difference of 100 MPa is observed between the **Ref** and **HE** materials for a constant lifetime. Among the second group, the **Rc** material shows a higher lifetime as compared to the other materials. Since this material experiences a comparable creep rate as compared to the other materials with the same fraction of oxide precipitates, this means that under creep conditions too, this material presents an improved ductility, as has been observed for the tensile tests. The test performed on the **Rc** material at 145 MPa is still ongoing. The recording of the strain being not accurate, it does not allow estimating the secondary creep rate.

4. DISCUSSION

4.1. Effect of the microstructure on tensile properties and creep resistance

Six model materials have been elaborated to understand the influence of microstructural parameters (grain size, nano-particles state, dislocation density) on the tensile properties in a wide temperature range (from room temperature to 800°C) and on creep resistance at 650°C.

The first result that needs to be discussed is the effect of the addition of nanometer-sized oxides (NOs) on the microstructure. In this study, only the un-strengthened material (**US**) presents martensitic areas. The presence of martensite has been observed in Fe-14Cr based alloys in some studies [40, 41]. It is due to the weak content of C or N, which impacts on the width of the γ and on the $\alpha + \gamma$ domains [42]. However, despite this presence of martensite, the **US** material constitutes a baseline for the impact of the other microstructural parameters.

The first effect of adding yttrium and titanium oxides is to drastically reduce the grain size and generate a bimodal (or multimodal) grain structure. As expected the proportion of small grains is highest when the fraction of NOs is highest, which corresponds to a more efficient pinning of the grain boundaries [5, 43-44].

Similarly to ref [13-14], the addition of yttrium and titanium oxides drastically improves the tensile properties however inducing a reduction of the total elongation, even reaching a brittle behavior for the **HS** material at room temperature. This effect of volume fraction of particles on the tensile properties has already been observed on ODS steels EUROFER 97 [45-46].

The effect of the volume fraction of NOs at comparable NO size can be evaluated by comparing the **LS**, **Ref** and **HS** materials. Whatever the temperature, yield strength evolves monotonically with volume fraction, with a ratio between the three materials remaining roughly constant. Concerning creep results, the three materials show a high apparent stress exponent, suggesting that the major effect of changing the NO volume fraction is a change in threshold stress. The situation for creep fracture time is more interesting, since the **LS** material, thanks to a higher ductility, shows a comparable dependence with stress as the **Ref** material, while the **HS** material stands higher in stress for a given time for fracture.

The effect of particle size of NOs can be evaluated by comparing the **Ref** and **CP** materials, with a doubling of the NO average size (and therefore a decrease by 8 of the NO density). At room temperature, the larger precipitate size induces a lower strength by about 300 MPa. However, this difference strongly decreases at 600°C to vanish and even invert at 800°C. Thus, even though the NOs have been shown to still be efficient obstacles at high temperature [47-48], these results show that aiming for an extremely small NO size may not be required for performance above 600°C. In terms of creep results, the **Ref** and **CP** materials also show comparable behaviors.

The effect of grain microstructure at comparable NO structure can be evaluated by comparing the **CP** and **Rc** materials. At room temperature, the two materials present similar yield strength, suggesting that the difference in average grain size is compensated by a small change in precipitate microstructure. At high temperature, the difference remains negligible in terms of yield strength. This may appear surprising since it is known that grain boundary sliding is activated at high temperature in the ODS steels presenting sub-micrometer size grains [48-50], which should be favoured in the **CP** material as compared to the **Rc** material. However, the tensile tests investigated here were realized at a relatively high strain rate, which probably prevents a control of yield strength by grain boundary sliding. Besides, the **Rc** material shows a significantly higher ductility at temperatures above

500°C, with a total elongation up to twice that of the **CP** material. It has actually been shown that different types of impurities and large precipitates can be present on the grain boundaries of ODS steel and promote damage accumulation during deformation at elevated temperatures [51-53]. This improvement is therefore likely related to the escape of the grain boundaries from these regions prone to damage formation during the recrystallization treatment. This behavior is similarly observed in creep: the **CP** and **Rc** materials show the same creep law, but the time to fracture in creep is larger in the **Rc** material. Thus, a recrystallized material may be a good candidate for improving the ductility during high temperature creep while maintaining a low creep rate.

Finally, the last parameter that needs to be discussed is the difference between the **Ref** (HIPed) and **HE** materials at comparable NO microstructure. At all temperatures, the **HE** material is observed to be stronger. The striking feature is that the difference in yield strength is constant with temperature (about 100 MPa). Thus, while at room temperature this difference amounts to less than 10% of the strength, it represents more than a factor of 2 at 800°C. The strength of the **HE** material even becomes higher than that of the **HS** material at this high temperature. Such a constant difference as a function of temperature (of the same order of magnitude, 100 MPa) has actually been observed by Serrano et al. [54] when comparing a **HE** material in the longitudinal and transverse directions, although Steckmeyer et al. [53] found a smaller difference for a similar study. As discussed by [53], the difference cannot be explained by the crystallographic texture only. Although we cannot rule out some effect of the morphological texture linked to the large grain present in the microstructure, both materials in our study (**Ref** and **HE**) present a large fraction of equiaxed sub-micrometer size grains, so that this difference has to be related to the change in dislocation density, which is still very high following the hot extrusion process [6], while it is low after hot isostatic pressing [55-56]. The contribution of forest dislocations is expected to decrease with increasing temperature because of thermally activated obstacle passing [57-58], and become small above 400°C, in contradiction with our results. Moreover, forest dislocations would affect strength equally in all directions, which would also be in contradiction with the anisotropy results of Serrano et al. [54]. However, the contribution of dislocations to yield strength is not only related to forest hardening, but it is also expected that the dislocation network, being the result of high temperature annealing (after processing), should be organized in such a way that most of the dislocations participate to long range internal stresses [59]. According to Kuhlmann-Wilsdorf [60], this internal stress scales as $\rho^{1/2}$, as for forest hardening, but with a smaller magnitude $\Delta\tau \approx \frac{\mu b}{2\pi}\sqrt{\rho}$. Considering the

dislocations densities in Table 2, the internal stress for the **Ref** material would be 95 MPa and that of the **HE** material 213 MPa. The difference is actually extremely close to the difference of strength observed between the two materials. As discussed in detail by Hervé [61], this internal stress cannot be overcome by thermal activation, so that its contribution should be constant with temperature, provided that the dislocation network does not experience recovery. Since hot extrusion occurred at 1150°C, it is likely that the remaining dislocation structure, stabilized by the presence of the NOs, is then stable over the complete temperature range from room temperature to 800°C. This explanation also supports the results of Serrano et al. [54] because these internal stresses are necessarily oriented, so that a strain path change from hot extrusion to tensile testing can be expected to be less influenced by the internal stresses as compared to testing in the same direction. This difference of the level of long-range internal stress between the **HE** and **Ref** materials, not only changes by the constant 100 MPa the strength over the complete temperature range, but also changes by the same amount (approximately) the creep stress at constant strain rate, the creep threshold stress, and the creep stress at constant time to fracture.

The best mechanical properties are exhibited by the **HE** material tested on the axial direction (parallel to the hot extrusion direction) with a good compromise between ductility and mechanical properties at high temperature. However it is known that extruded materials show poor mechanical properties in the transverse direction [54]. The second material which shows a good compromise between ductility and high temperature mechanical properties is the recrystallized ODS steel (**Rc**). Despite a decrease of mechanical properties at low temperature due to a larger precipitate mean radius, the mechanical properties are interesting at high temperature, and in particular under creep. Taking into account the results of the recent study of recrystallization of ODS steels [24], the mechanical properties of the **Rc** material could be further improved at lower temperature by avoiding the coarsening of NOs during the recrystallization process, using a larger rate of cold deformation and a lower recrystallization temperature.

4.2. Modeling of the yield strength at room temperature

All microstructural parameters contribute to the yield strength. Nanoparticles and dislocations are usually considered to be point obstacles. Thus, they are often described by a quadratic summation in a hardening model, contrary to the other microstructural parameters which are added linearly [62-63].

$$\sigma_y = \sigma_0 + \sigma_{ss} + \sigma_{GB} + (\sigma_{Disloc}^n + \sigma_{Particles}^n)^{1/n} \qquad \textbf{Equation 1}$$

where n=2, with σ_y the yield strength, σ_0 the Peierls-Nabarro's force, σ_{ss} the solid solution contribution, σ_{GB} the contribution of grain boundaries, σ_{Disloc} the dislocation forest hardening and $\sigma_{Particles}$ the contribution of nanoparticles. However, a quadratic addition law is oversimplified in the general case [64]. A recent study [65] has provided a phenomenological description of the dependence of the summation exponent n with the breaking angle of a dislocation pinned by point defect such as particles and dislocations.

$$n = 1 + e^{-\beta(\phi_{1c}+\phi_{2c})^{\delta}(\phi_{1c}-\phi_{2c})^{2m}} \quad \textbf{Equation 2}$$

where β, δ and m are adjusted parameters respectively equal to 0.1, 1 and 1 [65] and, ϕ_{1c} and ϕ_{2c} are the breaking angles corresponding to the two types of obstacles ($\phi_{1c} < \phi_{2c}$). In the present study the nanoparticles are considered to be impenetrable obstacles, whereas dislocations are relatively weak obstacles. Although the first hypothesis cannot be formally validated in all materials, its validity will be indirectly assessed by the success of the strength description. Considering the breaking angle of nanoparticles to be 5° (ϕ_{1c}) and the breaking angle of dislocation interactions to be 141° (ϕ_{2c}) [66], the summation exponent value n of equation 2 is equal to 1.24.

The Peierls-Nabarro stress (lattice resistance) is commonly expressed by the following equation:

$$\sigma_0 = \frac{2M\mu}{1-\nu}\exp\left(\frac{-2\pi a}{b(1-\nu)}\right) \quad \textbf{Equation 3}$$

where μ and ν are the shear modulus and the Poisson coefficient respectively, b the Burgers vector, M the Taylor factor and a the lattice parameter of pure iron.

Classically, the solid solution contribution σ_{SS} is estimated by the following form:

$$\sigma_{SS} = \sum K_i . {c_i}^z \quad \textbf{Equation 4}$$

With K_i a hardening constant and c_i the atomic fraction of the element i. The hardening parameters K of substitutional element such as W and Cr are estimated from [67]. According to Lacy & Gensamer and Susila et al., the exponent z is equal to ¾ for substitutional solid solution [68-69].

The Hall-Petch effect σ_{GB}, describing the contribution of grain boundaries, is generally inversely proportional to the square root of the mean grain size $\sigma_{GB} = \frac{k_{GB}}{\sqrt{D}}$ where k_{GB} is a microstructural parameter and D the mean grain size. Each oxide reinforced materials of this study shows a bimodal (or multimodal) microstructure. To get a more physical approach about the grain size strengthening, we used an extended Hall-Petch model, as done by Srinivasarao et al. [70]. This Hall-Petch modified model considers the material as a composite model with regions

of different strength as a function of their grain size and therefore corresponds to a summation weighted by the surface fraction (f_S) of each grain size (based on the surface distributions obtained with EBSD analyses). Thus:

$$\sigma_{GB} = \sum f_{Si} \frac{k_{GB}}{\sqrt{D_i}} \quad \textbf{Equation 5}$$

The forest dislocation hardening has been described by Taylor [71] with the following equation:

$$\sigma_{Dislo} = M\alpha\mu b \sqrt{\rho_{Dislo}} \quad \textbf{Equation 6}$$

Where α is a constant and ρ_{Dislo} is the dislocation density determined by TEM observations. At room temperature, we will consider that the internal stress contribution of the dislocation strengthening is included in this term.

Finally, the contribution of NOs was estimated with the Orowan modified equation proposed by Martin [72]:

$$\sigma_{Particles} = \frac{0.81\, M\mu b}{2\pi(1-\nu)^{\frac{1}{2}}} \frac{\ln\left(\frac{2\sqrt{\frac{2}{3}}r}{2b}\right)}{\left(\sqrt{\frac{2\pi}{3f}}r\right)} \quad \textbf{Equation 7}$$

Where r and f are the mean radius and volume fraction of nanoparticles listed for each model material in Table 2.

Using the equations of each of the above specified hardening contributions and the different parameters reported in Table 5, a very good agreement can be observed on Fig. 8 between the experimental yield strength and model result, taking into account the experimental uncertainties on the microstructural parameters. The histograms of Fig. 8 exhibit the contribution of each microstructural parameter. The contributions of dislocations and precipitates are their respective weight in the power-law addition of equation 1. As expected, one can note that the contribution, due to interaction between dislocations and nano-particles, increases with volume fraction of nano-particles. Indeed, it represents 379 MPa for **LS** material versus 959 MPa for **HS**. If we compare histograms of **Rc** and **CP**, one notices a significant difference of grain boundary strengthening. However, as observed on the tensile results (Fig. 5a), the histograms show that this difference is compensated by a difference in nano-particles strengthening.

Parameters	a	ν	b	M	μ	k_{GB}	K_{Cr}	K_W	α
	nm	-	nm	-	GPa	$MPa.\sqrt{m}$	$MPa.at\%^{-3/4}$	$MPa.at\%^{-3/4}$	-
References	[73]	[74]	[48, 74, 75]	[75]		[76]	[67]	[67]	[48]
Value	0.287	0.366	0.248	3	84	0.307	9.95	75.79	0.33

Table 5. Fixed parameters used for the strengthening model of every material.

4.3. Modeling of yield strength at elevated temperature

Because of the complexity of the microstructure and of the changes in deformation mechanisms that can occur in the different temperature ranges investigated here, we cannot expect to reach the same level of modeling for the

description of the evolution of mechanical properties with temperature. However, it is of interest to evaluate if a common framework can satisfactorily describe the evolution of yield stress with temperature in the different materials that we have investigated, which present a wide range of microstructures. The first parameter that varies with temperature is the elastic modulus. Since all equations describing strength contribution are directly proportional to the shear modulus, this variation accounts for part of the temperature dependence of yield strength. The evolution of Young's modulus with temperature is taken from [77] and shown in Table 6.

Based on the study of Alinger [57] and He [58], we then make the approximation that the contribution of forest dislocations is constant until 400°C and then equal to 0, and that the solid solution contribution follows the same trend but with a transition temperature of 600°C. Although these are clearly oversimplifications, these contributions are sufficiently limited so that uncertainties in these variations should not change the major conclusions of the current description. The grain boundary strengthening, however, is considered constant with temperature.

	20°C	**400°C**	**500°C**	**600°C**	**650°C**	**800°C**
Fe-14Cr-1W steel	213 ± 5	188 ± 5	179 ± 5	164 ± 5	155 ± 5	132 ± 5
Fe-14Cr-1W ODS	230 ± 5	205 ± 5	188 ± 5	175 ± 5	163 ± 5	132 ± 5

Table 6. Young's modulus of ferritic steel and ODS based Fe-14Cr-1W.

The most complicated temperature dependence to estimate is that of the precipitates. However, its evolution can be accessed experimentally by comparing the **HS** material, whose precipitation strengthening is largest, to the **US** material. Above 400°C, where the contribution of forest dislocations has cancelled, the difference between the **HS** and **US** materials is simply related to their difference in precipitation strengthening and grain size strengthening:

$$\sigma_{HS} - \sigma_{US} = \sigma_{(T)HS-Particles} + \sigma_{HS-GB} - \sigma_{US-GB} \qquad \textbf{Equation 8}$$

At room temperature, the difference becomes slightly larger to account for the difference in dislocation strengthening. From this strength difference, and taking into account the temperature variation of the Young modulus, it is possible to calculate the relaxation parameter k of the precipitation strengthening contribution proposed by Rösler and Arzt [78]:

$$\sigma_{(T)Particles} = \sqrt{1-k^2}\,\sigma_{Particles}$$

Based on this comparison, Table 7 gives the relaxation parameter estimated at the different temperatures. Now, it is possible to apply this relaxation parameter, along with the other strength contribution variations. The result of this evaluation is given in Fig. 9. This figure shows that a satisfactory description of every material is reached using this

description, with a slightly lower description quality when a large change of precipitate size occurs (**CP** and **Rc** materials), illustrating the fact discussed above that these larger precipitate containing materials outperform at higher temperatures the materials with smaller precipitates.

	500°C	**600°C**	**650°C**	**800°C**
k	0.45	0.92	0.96	0.99

Table 7. Relaxation factor k estimated using the Rösler & Arzt model.

This temperature dependent hardening model is a first approach whose purpose is to reproduce the main changes observed between the different materials. A more precise evaluation would require a much more detailed analysis, including progressive changes of all strengthening mechanisms as a function of temperature, and inclusion of strain rate dependence and internal stress. Particularly, as it is known that at slow deformation rates these ODS steels are susceptible to grain boundary sliding due to the presence of sub-micrometric grains [49-50], such a model would need to explicitly include a temperature and strain-rate dependence description of this phenomenon.

5. CONCLUSIONS

Using 7 model materials consolidated by HIP or HE, we have studied the influence of microstructural parameters (grain size, precipitation state, dislocation density) on the mechanical properties. We have shown that:

(i) The mechanical properties (creep and tensile) increase with the volume fraction of nano-particles however the ductility decreases and brittle behavior was observed at room temperature for the highest amount of particles.

(ii) The influence of nano-particles size is not very important above 600°C.

(iii) The recrystallized material presents good tensile properties at high temperature. Furthermore, the creep properties of the **Rc** material are very interesting due to their low creep rate and good ductility.

(iiii) The difference of internal stress between **HE** and **Ref** materials explains the constant difference of yield strength over all the temperature range.

Using the microstructural and mechanical characterization, a hardening model has been proposed to estimate the yield strength at room temperature. Taking account the evolution of deformation mechanisms with the temperature, this model has been extended for a large temperature range.

Acknowledgements

The authors would like to acknowledge Jean Luc Flament, Agathe Chauvin and Nicolas Boudier from CEA Saclay (FR), for the tensile tests and Dr. Michel Perez from INSA Lyon (FR) for fruitful discussion. G. Renou is thanked for help for the TEM-ACOM measurements.

References

[1] G.R. Odette, M.J. Alinger, B.D. Wirth, Recent developments in irradiation-resistant steels, Ann. Rev. Mater. Res. 38 (2008) 471-503.
[2] M. Laurent-Brocq, F. Legendre, M.H. Mathon A. Mascaro, S. Poissonnet, B. Radiguet, M. Loyer, O. Leseigneur, Influence of ball-milling and annealing conditions on nanocluster characteristics in oxide dispersion strengthened steels, Acta Mater. 60 (2012) 7150-7159.
[3] I. Hilger, X. Boulnat, J. Hoffmann, C. Testani, F. Bergner, Y. De Carlan, F. Ferraro, A. Ulbricht, Fabrication and characterization of oxide dispersion strengthened (ODS) 14Cr steels consolidated by means of hot isostatic pressing, hot extrusion and spark plasma sintering, J. Nucl. Mater. 472 (2016) 206-214.
[4] N. Sallez, P. Donnadieu, E. Courtois-Manara, D. Chassaing, C. Kübel, F. Delabrouille, M. Blat-Yrieix, Y. Bréchet, On ball-milled ODS ferritic steel recrystallization: From as-milled powder particles to consolidated state, J. Mater. Sci. 50 (2015) 2202-2217.
[5] X. Boulnat, N. Sallez, M. Dadé, A. Borbély, J.L. Béchade, Y. De Carlan, J. Malaplate, Y. Bréchet, F. De Geuser, A. Deschamps, P. Donnadieu, D. Fabrègue, M. Perez, Influence of oxide volume fraction on abnormal growth of nanostructured ferritic steels during non-isothermal treatments: An *in situ* study, Acta Mater. 97 (2015) 124-130.
[6] N. Sallez, X. Boulnat, A. Borbély, J.L. Béchade, D. Fabrègue, M. Perez, Y. De Carlan, L. Hennet, C. Mocuta, D. Thiaudière, Y. Bréchet, In situ characterization of microstructural instabilities: Recovery, recrystallization and abnormal growth in nanoreinforced steel powder, Acta Mater. 87 (2015) 377-389.
[7] J. Ribis, Y. De Carlan, Interfacial strained structure and orientation relationships of the nanosized oxide particles deduced from elasticity-driven morphology in oxide dispersion strengthened materials, Acta Mater. 60 (2012) 238-252.
[8] A.J. London, S. Santra, S. Amirthapandian, B.K. Panigrahi, R.M. Sarguna, S. Balaji, R. Vijay, C.S. Sundar, S. Lozano-Perez, C.R.M. Grovenor, Effect of Ti and Cr on dispersion, structure and composition of oxide nano-particles in model ODS alloys, Acta Mater. 97 (2015) 223-233.
[9] Y. Wu, J. Ciston, S. Kraëmer, N. Bailey, G.R. Odette, P. Hosemann, The crystal structure, orientation relationships and interfaces of the nanoscale oxides in nanostructured ferritic alloys, Acta Mater. 111 (2016) 108-115.
[10] B. Fournier, A. Steckmeyer, A.L. Rouffie, J. Malaplate, J. Garnier, M. Ratti, P. Wident, L. Ziolek, I. Tournie, V. Rabeau, J.M. Gentzbittel, T. Kruml, I. Kubena, Mechanical behaviour of ferritic ODS steels – Temperature dependancy and anisotropy, J. Nucl. Mater. 430 (2012) 142-149.
[11] B. Mouawad, X. Boulnat, D. Fabrègue, M. Perez, Y. De Carlan, Tailoring the microstructure and the mechanical properties of ultrafine grained high strength ferritic steels by powder metallurgy, J. Nucl. Mater. 465 (2015) 54-62.
[12] A. Chauhan, D. Litvinov, Y. De Carlan, J. Aktaa, Study of the deformation and damage mechanisms of a 9Cr-ODS steel: Microstructure evolution and fracture characteristics, Mater. Sci. Eng. A 658 (2016) 123-134.
[13] D.A. McClintock, M.A. Sokolov, D.T. Hoelzer, R.K. Nanstad, Mechanical properties of irradiated ODS-EUROFER and nanocluster strengthened 14YWT, J. Nucl. Mater. 392 (2009) 353-359.
[14] V. De Castro, J.M. Garces-Usan, T. Leguey, R. Pareja, Tensile and fracture characteristics of oxide dispersion strengthened Fe-12Cr produced by hot isostatic pressing, J. Nucl. Mater. 442 (2013) 119-123.
[15] A. Ramar, P. Spätig, R. Schäublin, Analysis of high temperature deformation mechanism in ODS EUROFER97 alloy, J. Nucl. Mater. 382 (2008) 210-216.
[16] R.L. Klueh, P.J. Maziasz, I.S. Kim, L. Heatherly, D.T. Hoelzer, N. Hashimoto, E.A. Kenik, K. Miyahara, Tensile and creep properties of an oxide dispersion strengthened ferritic steel, J. Nucl. Mater. 307-311 (2002) 773-777.
[17] I.S. Kim, B.Y. Choi, C.Y. Kang, T. Okuda, P.J. Maziasz, K. Miyahara, Effect of Ti and W on the mechanical properties and microstructure of 12% Cr base mechanical-alloyed nano-sized ODS ferritic alloys, ISIJ International 43 (2003) 1640-1646.
[18] A. Steckmeyer, M. Praud, B. Fournier, J. Malaplate, J. Garnier, J.L. Béchade, I. Tournié, A. Tancray, A. Bougault, P. Bonnaillie, Tensile properties and deformation mechanisms of a 14Cr ODS ferritic steel, J. Nucl. Mater. 405 (2010) 95-100.
[19] A. García-Junceda, M. Hernández-Mayoral, M. Serrano, Influence of the microstructure on the tensile and impact properties of a 14Cr ODS steel bar, Mater. Sci. Eng. A 556 (2012) 696-703.
[20] J.H. Schneibel, M. Heilmaier, W. Blum, G. Hasemann, T. Shanmugasundaram, Temperature dependence of the strength of fine- and ultrafine-grained materials, Acta Mater. 59 (2011) 1300-1308.
[21] M.C. Brandes, L. Kovarik, M.K. Miller, G.S. Daehn, M.J. Mills, Creep behavior and deformation mechanisms in a nanocluster strengthened ferritic steel, Acta Mater. 60 (2012) 1827-1839.
[22] S.Y. Zhong, V. Klosek, Y. De Carlan, M.H. Mathon, Modeling of structural hardening in oxide dispersion-strengthened (ODS) ferritic alloys, J. Mater. Sci. 51 (2016) 2540-2549.

[23] J.H. Kim, T.S. Byun, D.T. Hoelzer, C.H. Park, J.T. Yeom, J.K. Hong, Temperature dependence of strengthening mechanisms in the nanostructured ferritic alloy 14YWT: Part II – Mechanistic models and predictions, Mater. Sci Eng. A 559 (2013) 111-118.
[24] M. Dadé, J. Malaplate, J. Garnier, F. De Geuser, N. Lochet, A. Deschamps, Influence of consolidation methods on the recrystallization kinetics of a Fe-14Cr based ODS steel, J. Nucl. Mater. 472 (2016) 143-152.
[25] M. Praud, Plasticité d'alliages renforcés par nano-précipitation, PhD thesis, Université de Toulouse, 2012.
[26] X. Boulnat, Fast high-temperature consolidation of oxide-dispersion strengthened (ODS) steels: process, microstructure, precipitation, properties, PhD thesis, INSA Lyon, 2015.
[27] E.F. Rauch, M. Véron, Automated crystal orientation and phase mapping in TEM, Mater. Charact. 98 (2014) 1-9.
[28] F. De Geuser, A. Deschamps, Precipitate characterisation in metallic systems by small-angle X-ray or neutron scattering, C. R. Physique 13 (2012) 246-256.
[29] Z. Oksiuta, N. Baluc, Microstructure and Charpy impact properties of 12-14Cr oxide dispersion-strengthened ferritic steels, J. Nucl. Mater. 374 (2008) 178-184.
[30] C.C. Eiselt, M. Klimenkov, R. Lindau, A. Möslang, H.R.Z. Sandim, A.F. Padilha, D. Raabe, High-resolution transmission electron microscopy and electron backscatter diffraction in nanoscaled ferritic and ferritic-martensitic oxide dispersion strengthened-steels, J. Nucl. Mater. 385 (2009) 231-235.
[31] V. De Castro, T. Leguey, M.A. Auger, S. Lozano-Perez, M.L. Jenkins: Analytical characterization of secondary phases and void distributions in an ultrafine-grained ODS Fe-14Cr model alloy, J. Nucl. Mater. 417 (2011) 217-220.
[32] X. Boulnat, M. Perez, D. Fabrègue, T. Douillard, M.H. Mathon, Y. De Carlan, Microstructure evolution in nano-reinforced ferritic steel produced by mechanical alloying and spark plasma sintering, Metall. Mater. Trans. A 45 (2014) 1485-1497.
[33] H. Sakasegawa, L. Chaffron, F. Legendre, L. Boulanger, T. Cozzika, M. Brocq, Y. De Carlan, Correlation between chemical composition and size of very small oxide particles in the MA957 ODS ferritic alloy, J. Nucl. Mater. 384 (2009) 115-118.
[34] A. Deschamps, F. De Geuser, On the validity of simple precipitate size measurements by small-angle scattering in metallic systems, J. Applied Cryst. 44 (2011) 343-352.
[35] M. Dumont, L. Commin, I. Morfin, F. De Geuser, F. Legendre, P. Maugis, Chemical composition of nano-phases studied by anomalous small-angle X-ray: Application to oxide nano-particles in ODS steels, Mater. Charact. 87 (2014) 138-142.
[36] C.G. Panait, A. Zielińska-Lipiec, T. Koziel, A. Czyrska-Filemonowicz, A.F. Gourgues-Lorenzon, W. Bendick, Evolution of dislocation density, size of subgrains and MX-type precipitates in a P91 steel during creep and during thermal ageing at 600°C for more than 100000h, Mater. Sci. Eng. A 527 (2010) 4062-4069.
[37] P. Unifantowicz, Z. Oksiuta, P. Olier, Y. De Carlan, N. Baluc, Microstructure and mechanical properties of an ODS RAF steel fabricated by hot extrusion or hot isostatic pressing, Fus. Eng. Des. 86 (2011) 2413-2416.
[38] M.E. Kassner, Fundamentals of creep in metals and alloys, Elsevier, 2009.
[39] F.R. Larson, J. Miller, A time-temperature relationship for rupture and creep stresses, Trans. ASME 74 (1952) 765-775.
[40] M.A. Auger, V. De Castro, T. Leguey, A. Muñoz, R. Pareja, Microstructure and mechanical behavior of ODS and non-ODS Fe-14Cr model alloys produced by spark plasma sintering, J. Nucl. Mater. 436 (2013) 68-75.
[41] A. Karch, Etude des évolutions microstructurales lors de la transformation à chaud d'aciers ferritiques renforcés par dispersion d'oxydes, PhD thesis, Ecole National supérieure des mines de Paris, 2014.
[42] J. Baralis, G. Maeder, Précis Métallurgie, Nathan, 2005
[43] C. Cayron, E. Rath, I. Chu, S. Launois, Microstructural evolution of Y_2O_3 and $MgAl_2O_4$ ODS EUROFER steels during their elaboration by mechanical milling and hot isostatic pressing, J. Nucl. Mater. 335 (2004) 83-102.
[44] D.T. Hoelzer, J. Bentley, M.A. Sokolov, M.K. Miller, G.R. Odette, M.J. Alinger, Influence of particle dispersions on the high-temperature strength of ferritic alloys, J. Nucl. Mater. 367-370 (2007) 166-.172
[45] R. Lindau, A. Möslang, M. Schirra, P. Schlossmacher, M. Klimenkov, Mechanical and microstructural properties of a hipped RAFM ODS-steel, J. Nucl. Mater. 307-311 (2002) 769-772.
[46] R. Schaeublin, T. Leguey, P. Spätig, N. Baluc, M. Victoria, Microstructure and mechanical properties of two ODS ferritic/martensitic steels, J. Nucl. Mater. 307-311 (2002) 778-782.
[47] J. Malaplate, F. Mompiou, J.L. Béchade, T. Van Den Berghe, M. Ratti, Creep behavior of ODS materials: A study of dislocations/precipitates interactions, J. Nucl. Mater. 417 (2011) 205-208.
[48] M. Praud, F. Mompiou, J. Malaplate, D. Caillard, J. Garnier, A. Steckmeyer, B. Fournier, Study of deformation mechanisms in a Fe-14% Cr ODS alloy, J. Nucl. Mater. 428 (2012) 90-97.
[49] Y. Sugino, S. Ukai, B. Leng, Q. Tang, S. Hayashi, T. Kaito, S. Ohtsuka, Grain boundary deformation at high temperature tensile tests in ODS ferritic steel, ISIJ International 51 (2011) 982-986.
[50] H. Masuda, S. Taniguchi, E. Sato, Y. Sugino, S. Ukai, Two-dimensional observation of grain boundary sliding of ODS ferritic steel in high temperature tension, Mater. Trans. 55 (2014) 1599-1605.
[51] H. Sakasegawa, S. Ohtsuka, S. Ukai, H. Tanigawa, M. Fujiwara, H. Ogiwara, A. Kohyama, Microstructural evolution during creep of 9Cr-ODS steels, Fus. Eng. Des. 81 (2006) 1013-1018.
[52] R. Kasada, S.G. Lee, J. Isselin, J.H. Lee, T. Omura, A. Kimura, T. Okuda, M. Inoue, S. Ukai, S. Ohnuki, T. Fujisawa, F. Abe, Anisotropy in tensile and ductile-brittle transition behavior of ODS ferritic steels, J. Nucl. Mater. 417 (2011) 180-184.

[53] A. Steckmeyer, V.H. Rodrigo, J.M. Gentzbittel, V. Rabeau, B. Fournier, Tensile anisotropy and creep properties of a Fe-14CrWTi ODS ferritic steel, J. Nucl. Mater. 426 (2012) 182-188.
[54] M. Serrano, M. Hernández-Mayoral, A. García-Junceda, Microstructural anisotropy effect on the mechanical properties of a 14Cr ODS steel, J. Nucl. Mater. 428 (2012) 103-109.
[55] Z. Oksiuta, A. Ozieblo, K. Perkowski, M. Osuchowski, M. Lewandowska, Influence of HIP pressure on tensile properties of a 14Cr ODS ferritic steel, Fus. Eng. Des. 89 (2014) 137-141.
[56] Z. Oksiuta, P. Hosemann, S.C. Vogel, N. Baluc, Microstructure examination of Fe-14Cr ODS ferritic steels produced through different processing routes, J. Nucl. Mater. 451 (2014), pp. 320-327.
[57] M.J. Alinger, On the formation and stability of nanometer scale precipitates in ferritic alloys during processing and high temperature service, PhD thesis, University of California, 2004.
[58] P. He, On the structure-property correlation and the evolution of nanofeatures in 12-13.5% Cr oxide dispersion strengthened ferritic steels, PhD thesis, Karlsruhe Instituts für Technologie, 2013.
[59] J. Friedel, Dislocations, Pergamon Press, 1964.
[60] D. Kuhlmann-Wilsdorf, Theory of workhardening 1934-1984, Metall. Trans. A 16 (1985) 2091-2108.
[61] N. Hervé, Fluage d'aciers renforcés par dispersion nanométrique: caractérisation, modélisation et optimisation de la microstructure, PhD thesis, Université Grenoble-Alpes, 2016.
[62] U.F. Kocks, A.S. Argon, M.F. Ashby, Thermodynamics and kinetics of slip, Pergamon Press, 1975.
[63] G. Fribourg, Y. Bréchet, A. Deschamps, A. Simar, Microstructure-based modeling of isotropic and kinematic strain hardening in a precipitation-hardened aluminium alloy, Acta Mater. 59 (2011) 3621-3635.
[64] Y. Dong, T. Nogaret, W.A. Curtin, Scaling of dislocation strengthening by multiple obstacle types, Metall. Mater. Trans. A 41 (2010) 1954-1960.
[65] A. De Vaucorbeil, W.J. Poole, C.W. Sinclair, The superposition of strengthening contributions in engineering alloys, Mater. Sci. & Eng. A 582 (2013) 147-154.
[66] G. Monnet, L. Vincent, B. Devincre, Dislocation-dynamics based crystal plasticity law for the low- and high-temperature deformation regimes of bcc crystal, Acta Mater. 61 (2013), 6178-6190.
[67] M. Couvrat, Fabrication d'aciers ODS à haute performance: relation procédé, microstructure, propriétés mécaniques, PhD thesis, Université de Rennes 1, 2013.
[68] C.E. Lacy, M. Gensamer, The tensile properties of alloyed ferrites, Trans. ASME 32 (1944) 88-110.
[69] P. Susila, D. Sturm, M. Heilmaier, B.S. Murty, V. Subramanta Sarma, Effect of yttria particle size on the microstructure and compression creep properties of nanostructured oxide dispersion strengthened ferritic (Fe-12Cr-2W-0.5Y_2O_3) alloy, Mater. Sci. & Eng. A 528 (2011) 4579-4584.
[70] B. Srinivasarao, K. Ohi-ishi, T. Ohkubo, K. Hono, Bimodally grained high-strength Fe fabricated by mechanical alloying and spark plasma sintering, Acta Mater. 57 (2009) 3277-3286.
[71] G.I. Taylor, The mechanism of plastic deformation of crystals. Part I. - Theoretical, Proc. Roy. Soc. 145 (1934) 362-387.
[72] J.W. Martin, Micromechanisms in particle-hardened alloys, Cambridge University Press, 1980.
[73] M.A. Auger, V. De Castro, T. Leguey, M.A. Monge, A. Muñoz, R. Pareja, Microstructure and tensile properties of oxide dispersion strengthened Fe-14Cr-0.3Y_2O_3 and Fe-14Cr-2W-0.3Ti-0.3Y_2O_3, J. Nucl. Mater. 442 (2013) 142-147.
[74] T. Tanno, S. Ohtsuka, Y. Yano, T. Kaito, Y. Oba, M. Ohnuma, S. Koyama, K. Tanaka, Evaluation of mechanical properties and nano-meso structures of 9-11%Cr ODS steels, J. Nucl. Mater. 440 (2013) 568-574.
[75] A. Ramar, R. Schäublin, Analysis of hardening limits of oxide dispersion strengthened steel, J. Nucl. Mater. 432 (2013) 323-333.
[76] T.H. Courtney, Mechanical behavior of materials: second edition, Waveland Press, Illinois, 2000.
[77] T. Leblond, P. Olier, D. Nunes, D. Bossu, G. Loupias, Comparison of properties of extruded steels reinforced or not by Y-Ti-O nanoparticles, 3rd International Conference on Thermomechanical Processing of steels, Padova, 2008.
[78] J. Rösler, E. Arzt, A new model-based creep equation for dispersion strengthened materials, Acta Metall. Mater. 38 (1990) 671-683.

Figure(s)

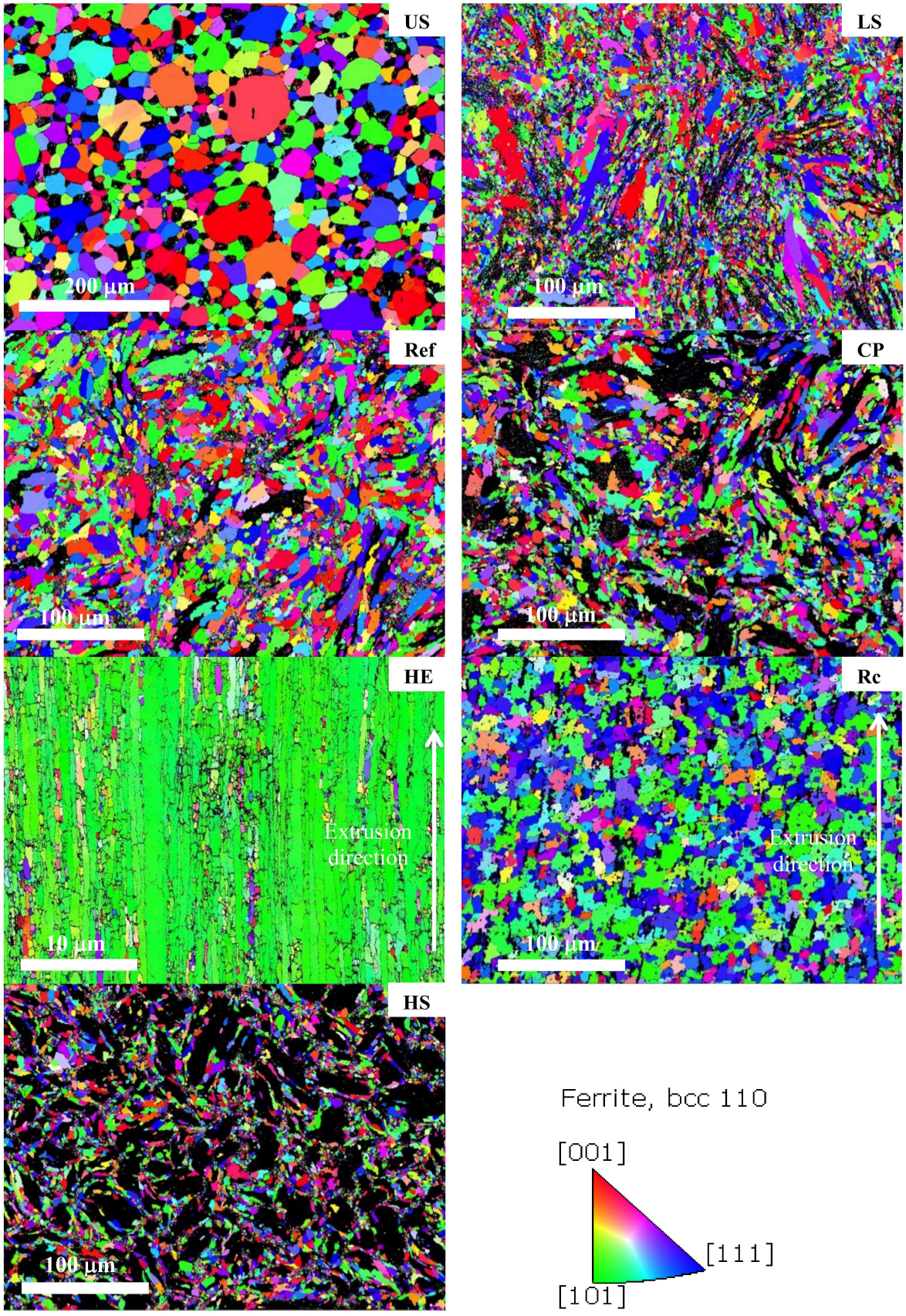

Fig. 1. EBSD maps of each model material and the standard triangle indicating correspondence between colors of the orientation imaging microscopy maps and crystallographic orientation.

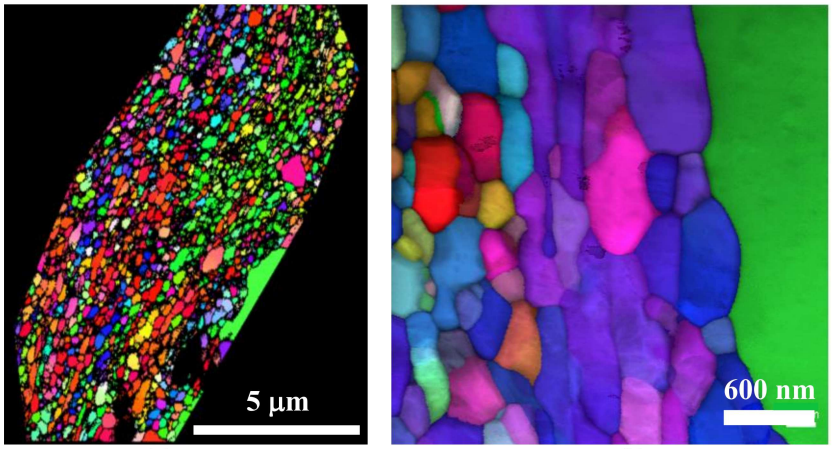

(a) (b)

Fig. 2. High-resolution EBSD (a) and ACOM-TEM (b) of the **Ref** material microstructure.

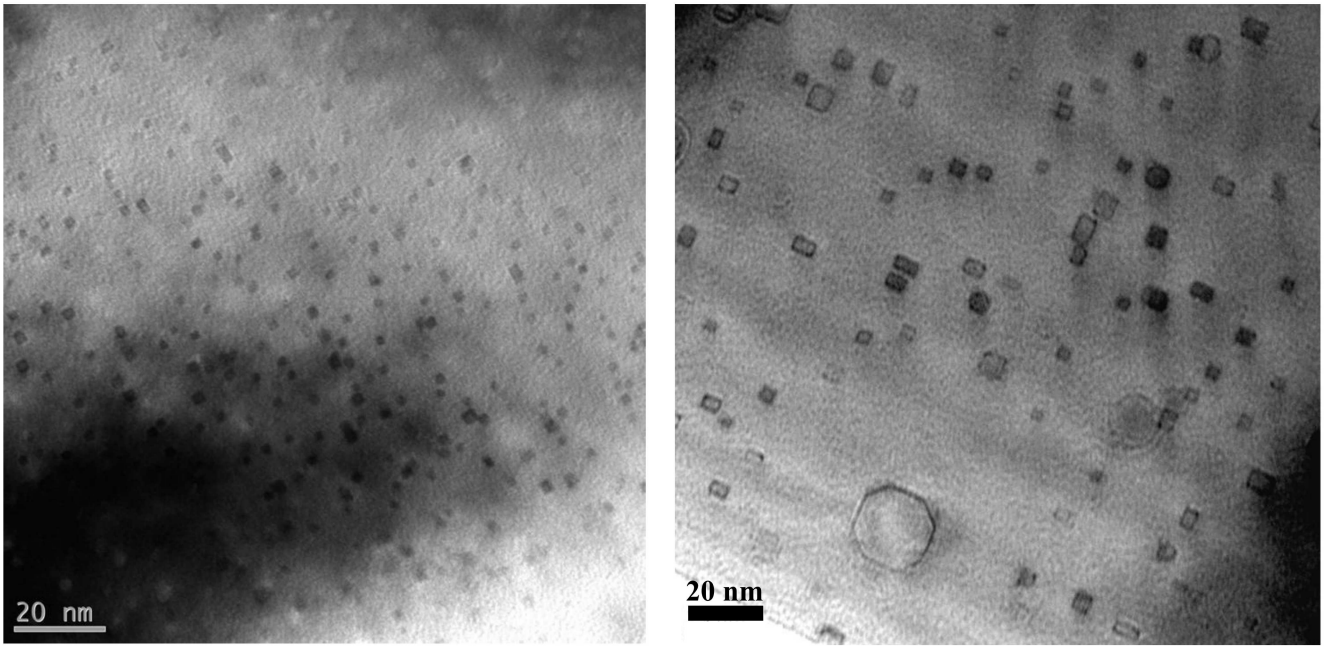

Fig. 3. TEM bright field images of precipitates state in the **Ref** material (a) and the **Rc** material (b)

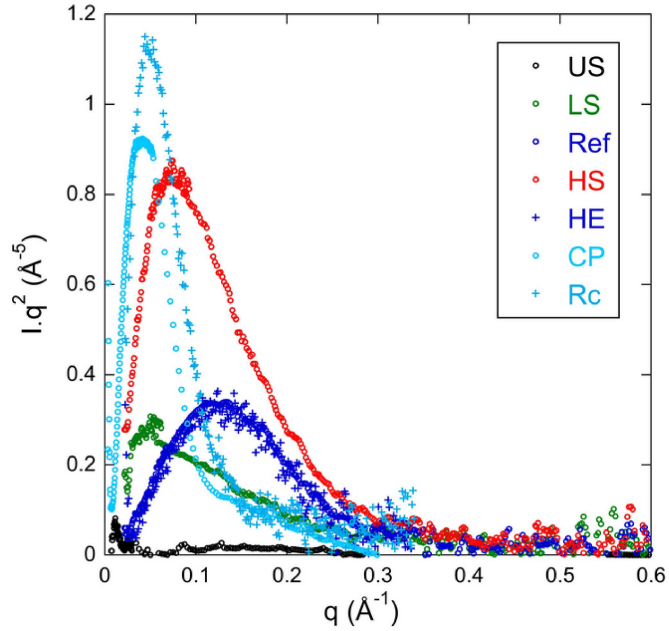

Fig. 4. Corrected SAXS intensity I vs the scattering vector q (a) and Kratky plot $I.q^2$ vs q for all materials.

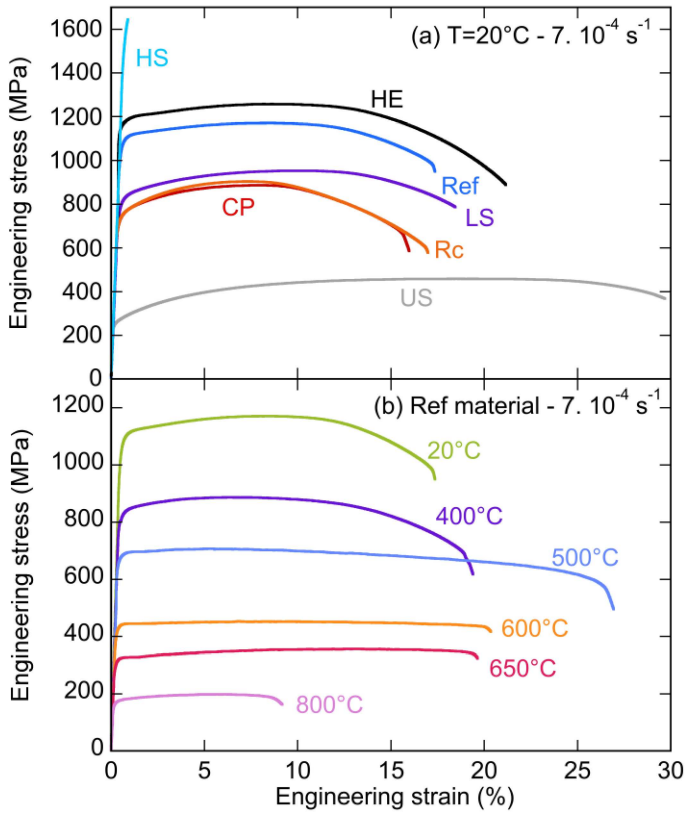

Fig. 5. (a) Engineering stress – strain curves for every material tested at room temperature with a strain rate of 7.10^{-4} s^{-1}. (b) Influence of testing temperature on the tensile properties of the **Ref** material with a strain rate of 7.10^{-4} s^{-1}.

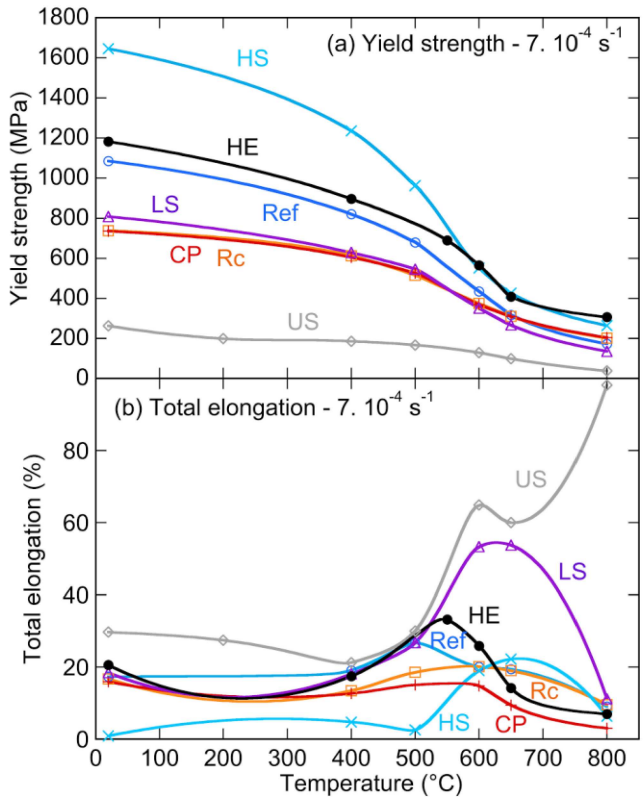

Fig. 6. (a) Evolution of the yield strength and (b) total elongation with temperature for all materials, at a strain rate of 7.10^{-4} s^{-1}. The uncertainties are respectively ± 5 MPa and ± 0.5%.

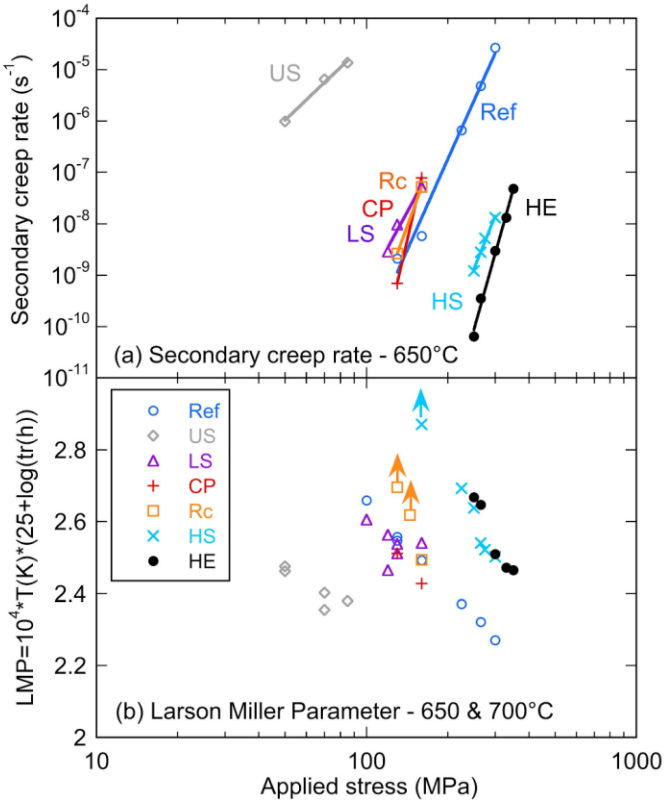

Fig. 7. Evolution of the secondary creep rate with the applied stress for every material tested at 650°C (a) and Larson Miller Parameter representation (b). The arrows symbolise the fact that the creep tests are still ongoing.

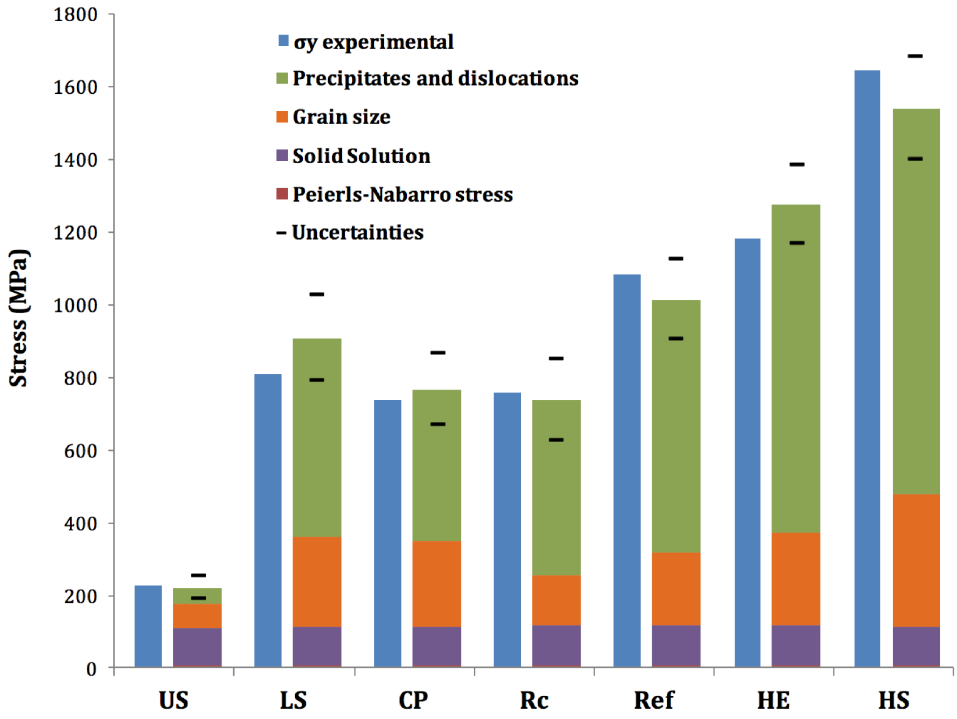

Fig. 8. Comparison between the experimental (blue histograms) and the estimated yield strength, representing by the different microstructural contribution at room temperature.

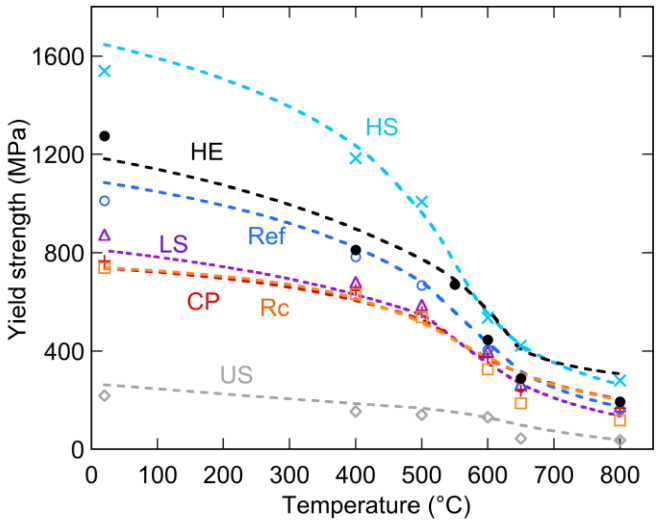

Fig. 9. Yield Strength modeling of every material on a large temperature range. The dotted lines correspond to the experimental yield strength while the square symbols draw yield strength estimated from the hardening model.